remote sensing

MDPI

Article

Subsidence Monitoring in Emilia-Romagna Region (Italy) from 2016 to 2021: From InSAR and GNSS Integration to Data Analysis

Gabriele Bitelli [1], Alessandro Ferretti [2], Chiara Giannico [2], Eugenia Giorgini [1,3,*], Alessandro Lambertini [1], Marco Marcaccio [4], Marianna Mazzei [4] and Luca Vittuari [1]

[1] Department of Civil, Chemical, Environmental, and Materials Engineering—DICAM, University of Bologna, 40136 Bologna, Italy; gabriele.bitelli@unibo.it (G.B.); alessandro.lambertini@unibo.it (A.L.); luca.vittuari@unibo.it (L.V.)
[2] Tre-Altamira, Ripa di Porta Ticinese 79, 20143 Milano, Italy; alessandro.ferretti@tre-altamira.com (A.F.); chiara.giannico@tre-altamira.com (C.G.)
[3] National PhD in Earth Observation, Sapienza University of Rome, 00185 Rome, Italy
[4] Agenzia Regionale Prevenzione e Ambiente (ARPAE) dell'Emilia-Romagna, Direzione Tecnica, 40122 Bologna, Italy; mmarcaccio@arpae.it (M.M.); mmazzei@arpae.it (M.M.)
* Correspondence: eugenia.giorgini@unibo.it

Abstract: This study investigates vertical soil movement, a subsidence phenomenon affecting infrastructure and communities in the Emilia-Romagna region (Italy). Building upon previous research—initially based on leveling and GNSS observations and later expanded with interferometric synthetic aperture radar (InSAR)—this study focuses on recent data from 2016 to 2021. A key innovation is the use of dual-geometry ascending and descending acquisitions to derive the vertical and the east–west movement components, a technique not previously applied at a regional scale in this area. The integration of advanced geodetic techniques involved processing 1208 Sentinel-1 satellite images with the SqueeSAR® algorithm and analyzing data from 28 GNSS permanent stations using the precise point positioning (PPP) methodology. By calibrating the InSAR data with GNSS measurements, we generated a comprehensive subsidence map for the study period, identifying trends and anomalies. The analysis produced 13.5 million measurement points, calibrated and validated using multiple GNSS stations. The final dataset, processed through geostatistical methods, provided a high-resolution (100-m) regional subsidence map covering nearly 11,000 square kilometers. Finally, the vertical soil movement map for 2016–2021 was developed, featuring isokinetic curves with an interval of 2.5 mm/year. The results underscore the value of integrating these geodetic techniques for effective environmental monitoring in subsidence-prone areas. Furthermore, comparisons with previous subsidence maps reveal the evolution of soil movement in Emilia-Romagna, reinforcing the importance of these maps as essential tools for precise subsidence monitoring.

Keywords: subsidence; InSAR; GNSS

check for updates

Academic Editors: Jie Shan, Cheng Zhong, Xiaoqiong Qin, Xuguo Shi and Wei Tang

Received: 15 January 2025
Revised: 19 February 2025
Accepted: 5 March 2025
Published: 7 March 2025

Citation: Bitelli, G.; Ferretti, A.; Giannico, C.; Giorgini, E.; Lambertini, A.; Marcaccio, M.; Mazzei, M.; Vittuari, L. Subsidence Monitoring in Emilia-Romagna Region (Italy) from 2016 to 2021: From InSAR and GNSS Integration to Data Analysis. *Remote Sens.* **2025**, *17*, 947. https://doi.org/10.3390/rs17060947

Copyright: © 2025 by the authors. Licensee MDPI, Basel, Switzerland. This article is an open access article distributed under the terms and conditions of the Creative Commons Attribution (CC BY) license (https://creativecommons.org/licenses/by/4.0/).

1. Introduction

1.1. The Subsidence Phenomenon and Monitoring Techniques

Land subsidence is the gradual sinking, or lowering, of the Earth's surface, driven by both natural and human-induced factors such as groundwater extraction, soil compaction, and geological processes [1–5]. This phenomenon can have significant consequences for infrastructure, agriculture, and local communities, increasing the vulnerability in regions

prone to subsidence [6–8]. Monitoring ground movements is therefore essential for effective urban planning, environmental protection, and disaster risk management [9–11]. Over time, subsidence monitoring techniques have advanced significantly, evolving from terrestrial surveying methods to modern remote sensing approaches and their integration [12–14]. Traditional methods, such as spirit leveling [15–17] and global navigation satellite systems (GNSS) [18,19], have long been used to assess ground deformation. More recently, remote sensing technologies like interferometric synthetic aperture radar (InSAR) [20,21] have gained prominence, offering high-precision, cost-effective monitoring over large areas.

Despite the substantial cost and time investment required, geometric leveling has historically been the primary source of subsidence data, relying on an extensive network of benchmarks. However, in recent years, GNSS technology has become increasingly widespread, with permanent GNSS stations now serving as a standard method for geodetic reference frame definition [22]. Additionally, GNSS stations play a crucial role in calibrating InSAR data [23,24]. Since InSAR operates within a relative reference system, calibration is necessary to align its observations with an absolute geodetic framework [25]. This process ensures that the InSAR time series and velocity estimates are accurately referenced to a predefined GNSS-based coordinate system [26–28]. Currently, integrating GNSS measurements with InSAR data has become a key approach for high-precision subsidence assessment at a regional scale [29–33]. In this context, the present study employs InSAR Sentinel-1 data in conjunction with GNSS observations to monitor subsidence, ensuring alignment with a well-established geodetic reference system.

1.2. The Emilia-Romagna Region

The Emilia-Romagna region is part of the Po River Plain, an area that has experienced natural subsidence for millions of years, a process that continues today [34]. The Apennine mountain range, which stretches from the northwest to the southeast of the region, is separated from the Emilia-Romagna Plain by a thrust system that causes the Apennines to uplift while the plain subsides. Additionally, the Quaternary cover of the lowlands undergoes slight folding due to tectonic thrusts between the Alps and the Apennines [35–37]. Over time, a series of geological processes have resulted in the deposition of sediments by watercourses. This process has led to the formation of extensive sedimentary systems at the outlets of these watercourses into the lowlands. These systems consist of alternating sandy and gravelly lenticular sediments, interspersed with finer clay deposits. The presence of highly compressible fine materials between more stable gravel and sand accumulations further contributes to ongoing subsidence [38–41]. This phenomenon has been the subject of rigorous study for decades [42]. While natural subsidence is primarily driven by the region's geological structure and the gradual compaction of fine sediments [43], human activities have significantly accelerated the process. Urbanization, land reclamation, and the extraction of subsoil fluids have all played a role [35]. Anthropogenic subsidence, particularly linked to fluid withdrawal from the subsoil, mainly groundwater and hydrocarbons, became evident in the 1950s, reaching its peak in the 1960s and 1980s [44]. Although the rate has decreased in recent decades, subsidence remains an ongoing issue [41,45,46]. The consequences of vertical ground movement in this region are profound, affecting infrastructure, economic activities, and the stability of natural ecosystems [6]. Given its significance, the quantitative assessment of subsidence in Emilia-Romagna has been the focus of numerous long-term studies [47–49].

1.3. Evolution of the Emilia-Romagna Subsidence Maps

In 1998, the Emilia-Romagna region, in collaboration with the Regional Agency for Environmental Protection of Emilia-Romagna (ARPAE) and the Department of Civil, Chem-

ical, Environmental, and Materials Engineering (DICAM) at the University of Bologna, established a regional subsidence monitoring network covering the entire plain. This network comprises a high-precision geometric leveling system with over 2300 reference points and approximately 60 GNSS stations [48]. The number of points was carefully determined to ensure adequate spatial distribution for both techniques, thereby enabling the accurate and reliable monitoring of the subsidence phenomenon. The first surveys were conducted in 1999, with about 50% of the leveling network remeasured in 2005. The difference in the number of measured leveling benchmarks, and consequently the length of the surveyed leveling lines located along the roads, was influenced by the need for a balance between the high costs associated with the leveling campaigns and the necessary spatial distribution of these lines to enable a meaningful comparison with SAR data. It is important to note that, in the meantime, the SAR technique had become a priority, proving to be both economically advantageous and reliable due to its calibration using GNSS stations. Data from the 1999 leveling campaign were compared with previous measurements, performed by different authorities for different purposes, leading to the creation of the first vertical ground movement map. The GNSS stations were resurveyed in 2002, providing additional insights into the local subsidence dynamics [49]. With the advent of satellite radar data in 1992, various SAR constellations were integrated with GNSS to periodically update the regional subsidence maps of the Po River Plain. ERS-1 and ERS-2 data were used for the period 1992–2000, Envisat and Radarsat for 2002–2006 [48], Radarsat-2 for 2006–2011 [47], and Radarsat-1/2 along with Cosmo-SkyMed for 2011–2016 [49]. Over time, the use of different SAR constellations introduced variations in the spatial resolution and revisit frequency. Previous studies derived the vertical ground motion from a single SAR acquisition orbit, calibrated with GNSS data [47]. This study, however, is the first to analyze the Emilia-Romagna region at a regional scale by combining both ascending and descending SAR acquisitions. To enhance the data accuracy, geostatistical interpolation methods were applied to create a dense 100 m × 100 m regular grid, followed by the generation of contour-based thematic maps using isokinetic isolines. Decades of experience in subsidence monitoring have undoubtedly contributed to the continuous advancement of these methodologies in the Emilia-Romagna region [47–49].

1.4. The 2016–2021 Emilia-Romagna Subsidence Map

The vertical movement map for the Emilia-Romagna region from 2016 to 2021, presented in this study, marks a significant advancement over previous analyses. The SAR data were acquired from the Sentinel-1 twin satellites, part of the Copernicus program [50–52], supported by the European Space Agency. Sentinel-1 provides comprehensive coverage of the entire region, spanning both lowland and mountainous areas, throughout the 2016–2021 period. Its shorter revisit time enabled high-frequency monitoring, while the dual-geometry processing of images—captured from both ascending and descending orbits—allowed for the determination of vertical (up) and horizontal (west–east) components of surface motion [53]. This study is the first to leverage both ascending and descending lines of sight (LOS) from Sentinel-1 to generate a regional-scale subsidence map for Emilia-Romagna. The methodological approach enabled the extraction of the up and east components of soil movement, providing a more comprehensive understanding of the ground deformation patterns. The datasets were calibrated using a regionally distributed network of GNSS stations, combined with an ad hoc calibration strategy. To ensure data reliability, an outlier rejection process was applied to mitigate local anthropogenic influences on subsidence. Finally, the validated and calibrated data were spatialized using geostatistical techniques on a 100 × 100 m grid, allowing for the creation of isokinetic contour maps of the vertical ground motion, with a resolution of 2.5 mm/year.

2. Materials and Methods

2.1. SAR Data and the SqueeSAR® Approach

The radar dataset comprises 1,208 Sentinel-1 satellite images, acquired in interferometric wide mode [54] from four different orbital tracks. These acquisitions provide full coverage of the Emilia-Romagna region from 2016 to 2021, with each track detailed in Table 1.

Table 1. Overview of the InSAR datasets analyzed. Data include images from four distinct satellite tracks, acquired along both ascending and descending orbits. The incidence angle values represent nominal values at mid-swath. The number of acquisitions may vary depending on the number of bursts processed.

Track	Orbit	Incidence Angle	Acquisitions	Period
T117	Ascending	39°	307	12 January 2016–26 June 2021
T95	Descending	40°	297–301	11 January 2016–25 June 2021
T15	Ascending	41°	288–293	17 January 2016–25 June 2021
T168	Descending	37°	306–307	16 January 2016–30 June 2021

The interferometric analysis of the InSAR dataset was conducted by TRE ALTAMIRA using the SqueeSAR® algorithm [55], applied to the ascending and the descending datasets. As is well known, the result of a multi-temporal InSAR analysis is a set of measurement points corresponding to coherent scatterers identified within the area of interest [56]. Each radar target is associated with a time series of displacement values estimated along the satellite's line of sight (LOS), along with its mean velocity, standard deviation, and temporal coherence. The analysis for the Emilia-Romagna region benefits from several improvements over the original SqueeSAR algorithm [55]. First, it employs an optimized, faster algorithm to estimate the optimal phase values of distributed scatterers (DS), leveraging a full coherence matrix derived from all possible image pair combinations. Second, it utilizes more advanced filtering techniques to mitigate atmospheric disturbances. In fact, even for highly reflective, stable radar scatterers (i.e., persistent or permanent scatterers), tropospheric and ionospheric effects can significantly corrupt phase measurements [25]. After 3D phase unwrapping, motion and atmospheric components are separated using a Model Order Selection (MOS) procedure [57], which allows for the adaptive modeling of displacement time series and improved filtering of the atmospheric phase screen in each interferogram. This approach enhances the estimation of non-linear motion components compared to traditional polynomial fitting methods, where the polynomial order must be predefined and remains fixed for all measurement points throughout the analysis. By combining InSAR datasets acquired from ascending and descending orbits, it is possible to estimate vertical and horizontal (east–west) displacement components. This is because modern satellite SAR sensors operate in near-polar orbits, with only a small deviation from the north–south axis, making InSAR relatively insensitive to motion in the north–south direction. Since different acquisition geometries observe, with a few exceptions, different objects, and each InSAR dataset contains distinct families of measurement points, the point clouds must be resampled onto a common spatial grid. Additionally, because the acquisition dates vary between datasets, displacement time series are interpolated and resampled onto a unified temporal grid. At the end of the resampling process, all InSAR datasets are aligned to the same spatial reference point and share a common temporal origin. For the present study, a grid of centroids spaced 50 m apart is chosen, and the measurements along the LOS provided by the radar targets located in the same cell are averaged, as shown in Figure 1. The projection matrix described in [53] is then inverted, assuming that the impact

of relative displacements along the north–south direction can be neglected, to derive both vertical and eastward displacement components.

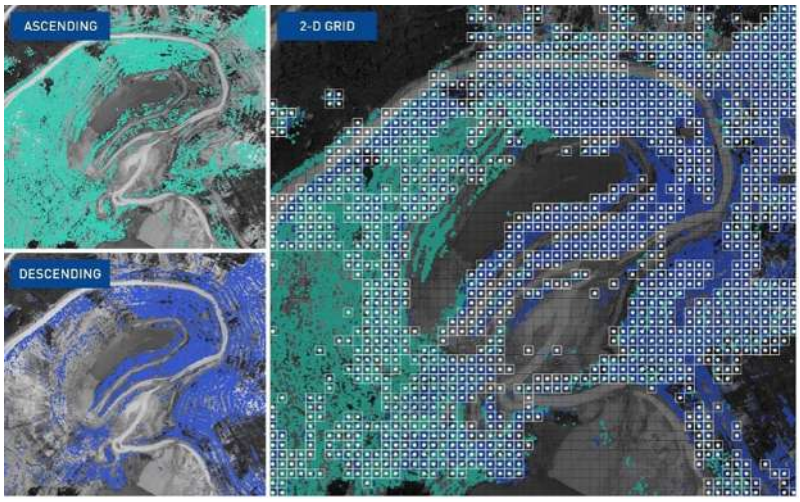

Figure 1. Two-dimensional measurements are estimated by subsampling ascending and descending data on a common spatial grid. The measurements of all points contained within the same cell are averaged to produce 2D measurement points located at the center of the cell. The 2D procedure only produces readings for cells containing points from both orbits (white cells).

The composition matrix described in [53] is then applied to derive both the time series and mean velocities for the up and east components. The north component is excluded due to the inherent limitations of the side-looking satellite acquisition geometry, which has significantly lower sensitivity to motion in the north–south direction [25].

2.2. GNSS Data and the PPP Approach

To achieve the comprehensive and precise management of the GNSS data, we opted to process the GNSS stations using a specialized software program for GNSS data processing. This approach ensured greater control over data processing, facilitating accurate calibration, validation, and consistency with geodetic reference frames. In this study, daily observations from 28 GNSS permanent stations (Figure 2) were analyzed to calibrate the InSAR data and validate the calibration process. Of these, 21 stations were selected for the calibration phase, ensuring homogeneous spatial coverage across the regional area, while 7 stations were used for validation. The validation stations were chosen either near GNSS stations used for calibration or in areas without stations, allowing for an assessment of the calibration's reliability under both conditions. The geographic coordinates of these stations are provided in Table A1.

The daily positions of the GNSS permanent stations were evaluated using the precise point positioning (PPP) approach [58]. This method allows for faster and less computationally intensive data processing than the traditional differential approach, while maintaining the same level of accuracy [59]. A key advantage of PPP is that it directly aligns the coordinates within a global reference system. After obtaining the daily data, the time series of positioning across the three components were analyzed to estimate the velocities in all three dimensions. The accuracy of three-dimensional coordinate variations over time for permanent stations is typically within a few tenths of a millimeter per year, which requires data collection spanning at least 2.5 years to account for periodic seasonal effects [60,61]. The PPP approach was implemented using the GIPSYX 1.7 software package (https://gipsy.jpl.nasa.gov, (accessed on 10 January 2022)) to analyze the Rinex data recorded from 2016 to 2021. Key processing parameters included the Vienna Mapping Function (VMF) [62] as the tropospheric model, a cut-off angle of 10°, and the absolute

calibration of the antenna phase center variations using the models from the IGS absolute correction file, igs14.atx (https://cddis.nasa.gov/Data_and_Derived_Products/GNSS/GNSS_product_holdings.html, (accessed on 10 January 2022)). Non-fiducial products from the Jet Propulsion Laboratory (JPL) were used for satellite orbits. The results from GIPSYX were then transformed into the International Terrestrial Reference System (ITRS) using a set of local Helmert transformation parameters derived from a regional network of 20 GNSS permanent stations. This network includes stations from the International GNSS Service (IGS, https://network.igs.org, (accessed on 10 January 2022)) and from the IAG Reference Frame Sub-Commission for Europe (EUREF, https://epncb.oma.be, (accessed on 10 January 2022)), as shown in Figure 3. The ITRF coordinates were then transformed into ETRF to remove the Eurasian plate motion using the parameters published by Z. Altamimi (Table 3) in the corresponding technical note [63]. The final products were the time series in the north, east, and up components of the GNSS stations, along with the relative mean velocities.

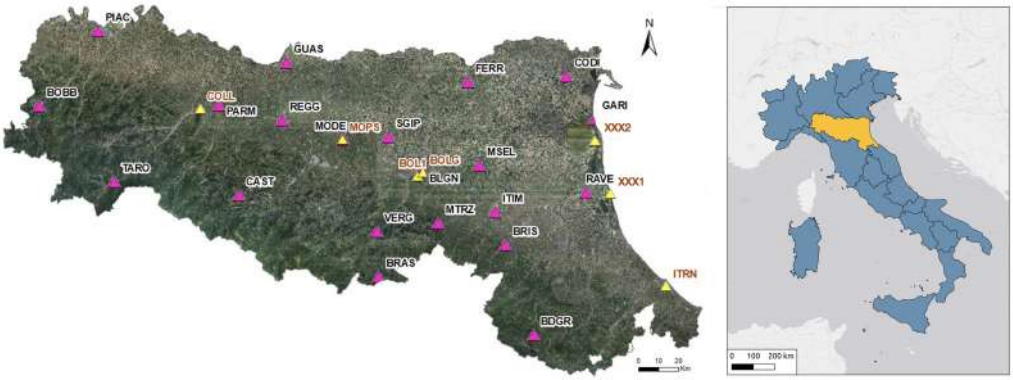

Figure 2. On the (**left**), the locations of the 21 GNSS permanent stations used for calibration (pink triangles) and of the 7 stations used for post-calibration (yellow triangles). On the (**right**), the map of the Italian regions with Emilia-Romagna highlighted.

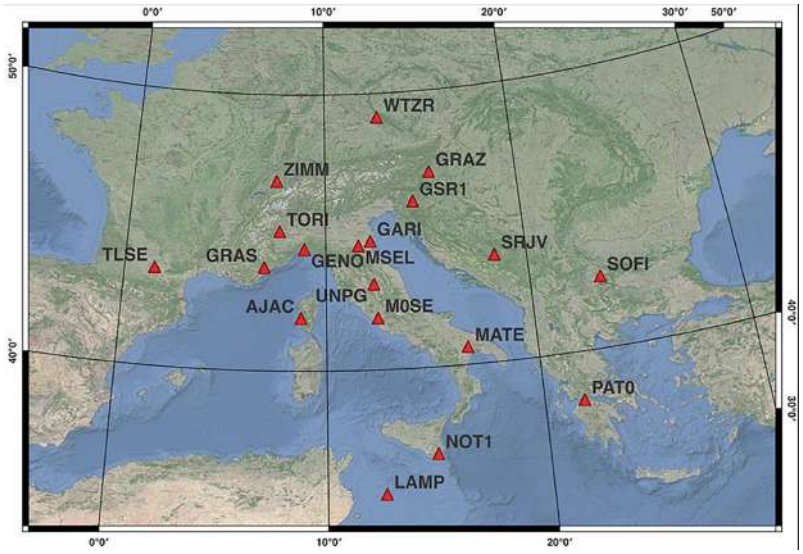

Figure 3. The IGS/EUREF geodetic stations composing the regional network, identified with the international codes.

2.3. InSAR Calibration

InSAR and GNSS are complementary techniques for the monitoring of surface movement, and their integration is employed to leverage the strengths of both technologies in terms of spatial density, precision, and accuracy. By combining InSAR and GNSS mea-

surements, a high spatial density of information is obtained with optimal precision and accuracy, provided that both datasets are aligned to a common reference system. InSAR data, initially aligned in a relative reference system [27], require calibration to an absolute reference system for absolute results. This is true whether the data are represented in terms of LOS or planimetric components [64]. The InSAR calibration workflow used in the present study is outlined in Figure 4 and described in detail below.

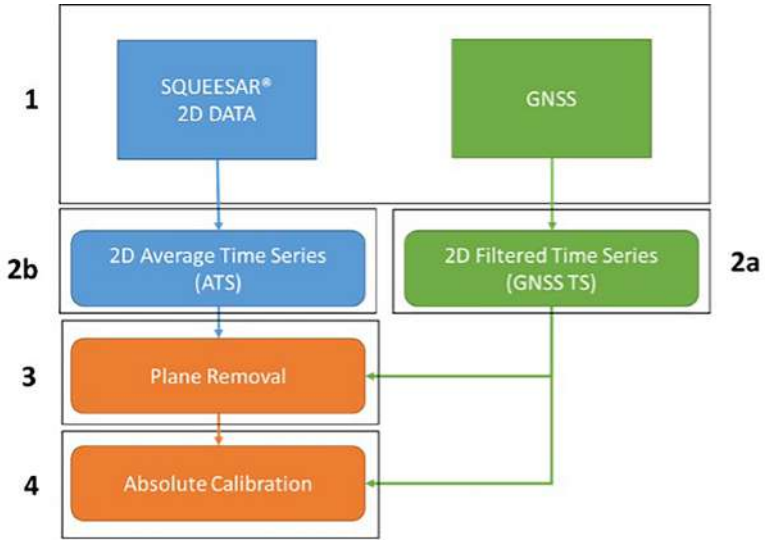

Figure 4. InSAR calibration process. The blue blocks refer to the InSAR dataset, the green blocks refer to the GNSS dataset, and the orange blocks contain the step in which the InSAR and the GNSS datasets are integrated.

2D—average InSAR time series. Generally, GNSS benchmarks and InSAR points are not perfectly co-located, and the accuracy of the InSAR point location is typically within a few meters, while GNSS benchmark locations are known with centimeter-level precision. Due to this disparity, InSAR measurement points within a certain radius of each GNSS benchmark are selected. These selected points are then used to calculate an average time series that will be compared with the corresponding GNSS time series. This approach ensures that data collected at the same location, over the same period, can be directly compared for accuracy and consistency.

2D—filtered time series. Generally, the time sampling of GNSS data differs from that of InSAR. To address this, the GNSS time series are filtered using a moving window, which includes data from several days before and after each SAR acquisition date. This method ensures that the GNSS data are aligned with the InSAR measurements, improving the accuracy of the comparison between the two datasets.

Plane removal. The difference in the average velocity is calculated for each average time series and the corresponding GNSS data. To calibrate the InSAR measurements, a first-order surface (plane) is statistically estimated at the regional scale by minimizing the residuals between the average time series and the corresponding GNSS. This plane is then removed from all InSAR measurement points. Since the plane alignment only accounts for a linear regional trend, additional calibration is performed to account for potential non-linear regional trends. This is achieved by deriving a unique common residual series at the regional scale, based on the residuals between the individual measurement points and the GNSS. The resulting residual time series reflects the movement of the local InSAR reference points relative to the global GNSS reference frame. Finally, this residual time series is removed from each individual InSAR measurement point time series, ensuring more accurate calibration across the entire dataset.

Absolute calibration. The obtained InSAR data, after the removal of the plane and the calibration of the time series, are then aligned to the same GNSS reference system. In this case, the data are referenced to the ETRF2000 intraplate reference system. This alignment ensures that the InSAR results are consistent with the GNSS reference frame, providing a unified and accurate representation of surface movements across the region.

3. Results

The following analysis encompasses InSAR processing, calibration, verification, and the final production of the Emilia-Romagna subsidence map. The interferometric analysis results were applied using a novel approach, differing from the methodology employed in the previous survey campaign, which covered the period from 2011 to 2016. This updated approach introduces improvements in precision and spatial coverage, contributing to a more accurate and comprehensive assessment of subsidence in the region [49]. The data used in this work were as follows:

- The mean velocities and the time series of the GNSS permanent stations, obtained from the precise point positioning approach;
- The LOS and east–up results of the SqueeSAR® interferometric analysis;
- The basic cartographic data and database of high-resolution satellite images.

The main aspects of the study include the definition of a velocity datum for the interferometric analysis and the subsequent verification of its effectiveness during the calibration phase of the interferometric data. Additionally, the study included a statistical analysis of the spatial distribution and type of measurement points, as well as the implementation of screening procedures to identify and remove any outliers. The entire dataset was validated to ensure the reliability of the results. Finally, the velocities derived from the interferometric analysis were interpolated to create a raster model of the vertical ground motion velocities for the Emilia-Romagna plain area, along with the mapping of isokinetic curves.

3.1. InSAR Measurement Points and East–West Components

The SqueeSAR® analyses resulted in a total of 13,555,277 measurement points (MP) across the entire Emilia-Romagna region (Figure 5). For each MP, displacement time series were generated, representing the evolution of the displacement for each acquisition date, measured along the LOS direction. Additionally, the annual average displacement rate for each MP was also calculated and provided.

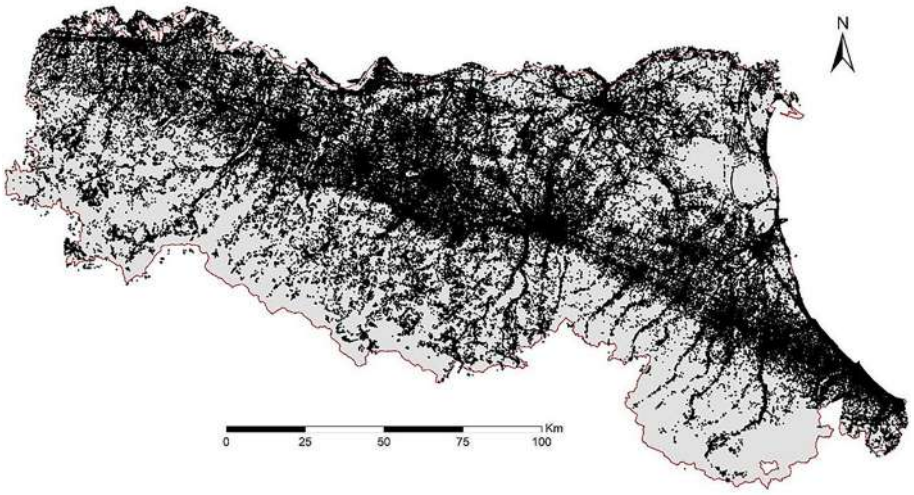

Figure 5. Distribution of Sentinel-1 MP, resulting from the SqueeSAR® interferometric analysis.

The density and distribution of the MP identified by the analysis are influenced by several factors, including the resolution of the imagery, surface characteristics, changes over time, and topography of the region. The highest densities of MP are found in urbanized areas, built-up regions, and locations with man-made infrastructure. In contrast, cultivated and vegetated areas generally exhibit much lower MP densities. To calculate the vertical and horizontal movement components, radar measurement points for each LOS were resampled and averaged onto a regular grid with 50 m × 50 m points (pseudo-MP). This process involved applying the decomposition matrix, which incorporates the satellite's incidence and heading angles. The resulting mean velocities, derived from combining the ascending and descending LOS in both the up and east–west directions, are presented before the calibration process in Figures 6 and 7.

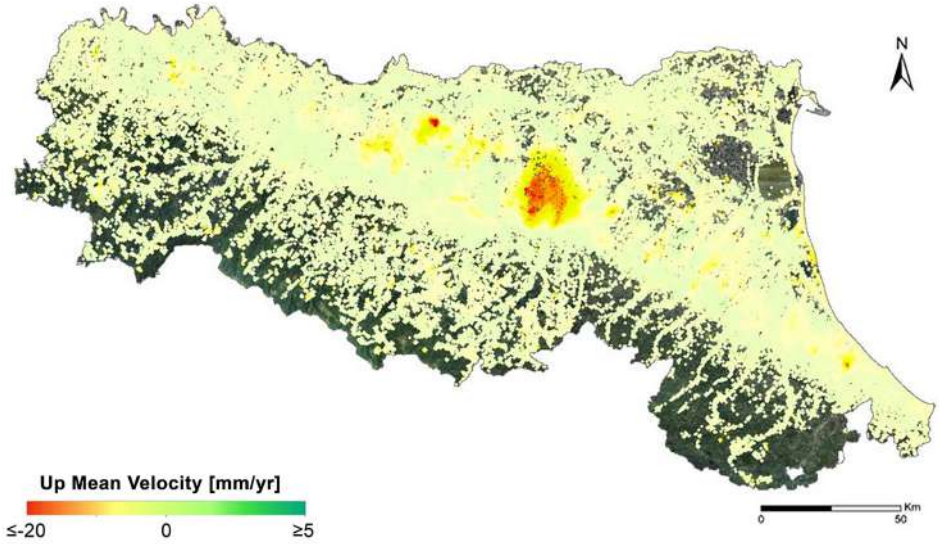

Figure 6. SqueeSAR® MP mean velocity along the up component, expressed in mm/yr.

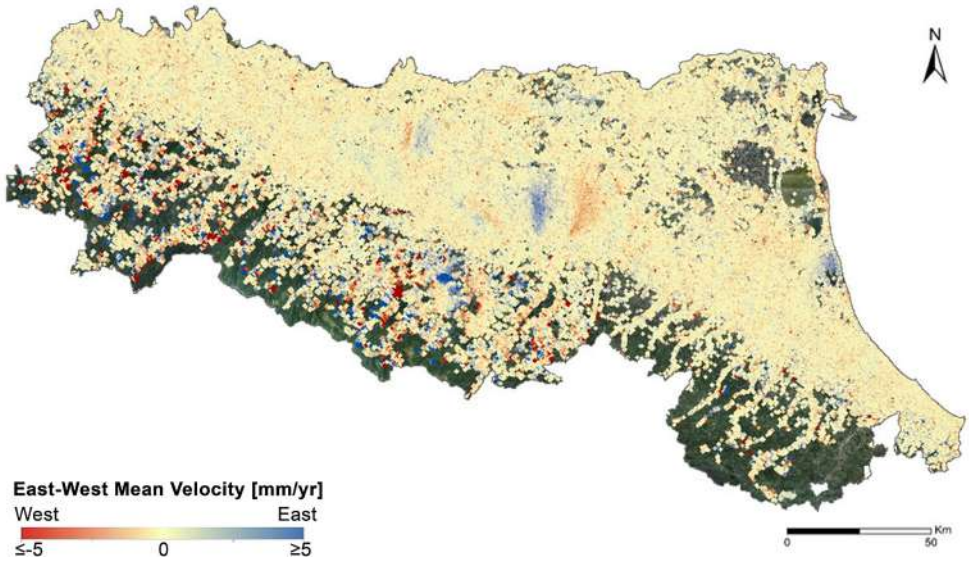

Figure 7. SqueeSAR® mean velocity along the east–west component, expressed in mm/yr.

3.2. GNSS Mean Velocities and Time Series in ETRF

Table 2 presents the north, east, and vertical up velocity components for each GNSS station within the Emilia-Romagna region under investigation, along with the associated mean square deviations. The uncertainties (sigma) shown in Table 2 were calculated using the

RealSigma option implemented within the TSVIEW package [65] for the GAMIT-GLOBK (MIT) GNSS analysis software (http://geoweb.mit.edu/~tah/GGMatlab/ (accessed on 10 January 2022)). This approach employs an autocorrelated noise model for the time series, rather than assuming white noise, thus avoiding the assumption of temporally independent errors. This is achieved by calculating the reduced chi-squared statistic (chi-squared per degree of freedom) for increasingly longer time averages of the residuals. Autocorrelation is estimated by identifying the point at which the reduced chi-squared statistic begins to increase significantly with the averaging time. The RealSigma option yields more realistic and conservative uncertainty estimates. These uncertainties are larger than those obtained under the white noise assumption because the autocorrelated noise model accounts for the increased inherent uncertainty in the data due to temporal error correlations. These velocities are expressed in the ETRF2000 intraplate reference system. The table includes data from both the 21 GNSS stations used to calibrate the interferometric data and the 7 GNSS stations used for the a posteriori verification of the interferometric results. This detailed dataset allows for the comparison and validation of the InSAR-derived velocities and provides insights into the accuracy of the calibration process applied to the satellite-based measurements. The markers for stations XXX1 and XXX2 have been modified because they do not belong to public GNSS networks.

Table 2. GNSS north, east, and up velocities and the relative standard deviation of the time series with respect to the linear trend of each component.

Marker	V_N [mm/yr]	σ V_N [mm/yr]	V_E [mm/yr]	σ V_E [mm/yr]	V_U [mm/yr]	σ V_U [mm/yr]
Calibration						
BGDR	2.1	0.04	0.24	0.03	0.98	0.05
BLGN	5.68	0.02	−0.81	0.02	−8.25	0.05
BOBB	1.09	0.01	0.31	0.01	−0.54	0.04
BRAS	1.65	0.02	0.09	0.01	0.48	0.04
BRIS	3.41	0.02	1.09	0.01	0.63	0.05
CAST	1.76	0.02	0.09	0.01	0.83	0.05
CODI	2.19	0.01	0.01	0.01	−2.81	0.03
FERR	2.56	0.01	0.39	0.01	−1.12	0.03
GARI	1.29	0.01	−0.28	0.01	−2.75	0.04
GUAS	1.81	0.01	0.1	0.01	−1.65	0.05
ITIM	3.46	0.01	0.82	0.01	−0.37	0.03
MODE	2.83	0.01	0.82	0.01	−4.1	0.04
MSEL	2.81	0.01	0.92	0.01	−1.83	0.03
MTRZ	3.83	0.02	1.57	0.02	−0.85	0.08
PARM	1.86	0.01	0.75	0.01	−0.3	0.05
PIAC	1.41	0.01	0.16	0.01	−0.71	0.03
RAVE	2.94	0.01	0.31	0.01	−3.75	0.04
REGG	2.35	0.01	−0.23	0.01	−3.12	0.04
SGIP	3.11	0.01	1.49	0.02	−6.97	0.04
TARO	1.12	0.01	0.29	0.01	−0.58	0.05
VERG	2.53	0.01	1.86	0.01	1	0.05
Validation						
BOL1	4.17	0.02	0.37	0.01	−0.32	0.04
BOLG	4.14	0.02	0.32	0.02	−2.04	0.06
COLL	1.59	0.02	1.25	0.02	−2.33	0.05
XXX1	2.39	0.01	3.27	0.02	−8.71	0.04
ITRN	3.94	0.01	0.95	0.03	−1.23	0.04
MOPS	3.17	0.01	0.73	0.02	−3.92	0.04
XXX2	2.7	0.02	−0.6	0.02	−3.72	0.06

3.3. Calibration of SqueeSAR® Pseudo-MP

To align the SqueeSAR® results (up and east–west components) with the ETRS, the calibration process requires the use of the GNSS station network outlined in Section 2.2. This alignment is achieved by utilizing both the average velocity from the GNSS time series and the relative time series, following the calibration workflow described in Figure 4. To ensure spatial correspondence between the GNSS stations and the nearby radar targets, only InSAR points within a 100 m radius of the GNSS station are selected. From these, the five highest-quality targets are identified and used to calculate the mean time series. This mean time series is then compared with the time series from the nearest GNSS station, after filtering the GNSS data using a 21-day moving window (spanning 10 days before and after each SAR acquisition date). The time series of the difference between the averaged SqueeSAR® data and the GNSS data is evaluated. The next step in the calibration process involves assessing and subtracting the averaged difference time series from the SqueeSAR® targets. As a result, the final calibrated InSAR data are aligned with the same reference system as the GNSS permanent station network. The plain values and the residual time series that were removed for calibration are provided in Tables A2 and A3. Table 3 summarizes the calibration accuracy achieved, showing that the vertical and horizontal velocity residuals between the InSAR and GNSS measurements are less than 1 mm/year on average. This performance aligns with the expected accuracy of these high-precision monitoring techniques [66].

Table 3. GNSS mean velocity (mm/yr), SqueeSAR® post-calibration mean velocity (mm/yr), and residuals with respect to the GNSS mean velocity (mm/yr), for the up and east components.

Marker	V_U GNSS [mm/yr]	V_U SqueeSAR® [mm/yr]	ΔV_U [mm/yr]	V_E GNSS [mm/yr]	V_E SqueeSAR® [mm/yr]	ΔV_U [mm/yr]
BGDR	0.9	-	-	0.2	-	-
BLGN	−8.3	−7.5	1	−0.9	−1.4	−0.5
BOBB	−0.6	0	0.6	0.3	0.5	0.2
BRAS	0.5	−0.9	−1.4	0	0.3	0.3
BRIS	0.6	-	-	1.1	-	-
CAST	0.8	−0.6	−1.4	0	−0.1	−0.1
CODI	−2.8	−3.1	−0.3	0	0.1	0.1
FERR	−1	−2.4	−1.4	0.4	0.4	0
GARI	−2.8	−2.9	−0.1	−0.3	0.1	0.4
GUAS	−1.6	−1.8	−0.2	0.1	0.2	0.1
ITIM	−0.4	−1.3	−1	0.8	0.3	−0.5
MODE	−4.4	−2.6	1.8	0.8	0.3	−0.5
MSEL	−1.9	−0.3	1.6	0.9	1	0.1
MTRZ	0	-	-	1.5	-	-
PARM	−0.1	−0.5	−0.7	0.8	0.5	−0.2
PIAC	−0.7	−1.5	−0.8	0.1	0.2	0
RAVE	−3.8	−3.1	0.7	0.3	0.4	0.1
REGG	−3.2	−1.9	1.2	−0.2	0.7	0.9
SGIP	−7	−5.6	1.4	1.5	1.8	0.3
TARO	−0.6	−0.7	−0.1	0.2	0.5	3
VERG	0.7	−0.6	−1.3	1.8	1	−0.8

3.4. Validation of SqueeSAR® Calibrated Up and East–West Mean Velocities

Following the calibration of the SqueeSAR® dataset, the results were validated by comparing the velocities from the calibrated SqueeSAR® data with those from GNSS stations that were not involved in the calibration stage. To conduct this validation, two pseudo-MP capture radii around the GNSS stations were chosen: 100 m and 250 m. The velocities of the pseudo-MP falling within these buffer areas were averaged, and the

resulting velocities were then compared with the velocities from the GNSS stations. The mean residual over the seven blind control points was found to be

- 0.17 mm/year, with a standard deviation of 1.3 mm/year, for the 100 m capture radius;
- 0.01 mm/year, with a standard deviation of 1.3 mm/year, for the 250 m capture radius.

Overall, for the 100 m radii case results, reported in Table 4, the velocity differences obtained are smaller than the accuracy provided by the SqueeSAR® data, validating the calibration process (for the station showing the greatest difference, a heterogeneity was found in the values of the surrounding pseudo-MP points).

Table 4. Validation of the calibrated SqueeSAR up component. In the table, for the 100 m radii, we reported the GNSS station marker name, the GNSS mean up velocity [mm/yr], the pseudo-MP up mean velocity [mm/yr], and the difference between the SqueeSAR and GNSS up velocities [mm/yr].

Marker	V_U GNSS [mm/yr]	V_U SqueeSAR® [mm/yr]	ΔV_U [mm/yr]
BOL1	−0.3	−1.8	1.5
BOLG	−2	−2.8	0.8
COLL	−2.3	−1.1	−1.2
XXX1	−8.7	−6.7	−2
ITRN	−1.2	−2.2	1
MOPS	−3.9	−2.7	−1.2
XXX2	−3.7	−3.7	0

The sample examined, although limited, includes a total of 21 permanent GNSS stations distributed across the analysis area, in addition to the seven stations used for the blind validation of the results following calibration. The values obtained from this validation process can be considered entirely satisfactory, reinforcing the methodology's reliability. Based on this validation, an overall uncertainty threshold of approximately ±2 mm/year was assigned to the displacement velocity analysis. Given this uncertainty threshold, it was decided to represent the results in the final cartography with isokinetic curves spaced at intervals of 2.5 mm/year. This approach aligns the current dataset with the precision observed in the previous analysis conducted during the 2011–2016 period. Following the successful validation and calibration of the data, both the vertical and horizontal (east–west) velocity time series were integrated into a georeferenced database. The results were then visualized and are presented in Figures 8 and 9, which show the aligned displacement velocities for the region under study.

The map of the east–west horizontal mean velocities (Figure 9) represents an important new feature in the updated subsidence cartography, distinguishing this monitoring campaign from the previous one (2011–2016). The map helps to highlight—particularly in the lowland areas, where significant vertical ground movements are present—the associated horizontal movements. In these regions, the horizontal movements predominantly move eastward in the Bologna, Reggio Emilia, and coastal areas (such as the mouth of the Fiumi Uniti and Lido di Dante). Conversely, a westward direction is observed in parts of the Reggio Emilia and Bologna areas. In the hilly and mountainous regions, the influence of tectonic and gravitational processes contributes to more pronounced variability and intensity in the horizontal movements. This contrasts with the plains, where the horizontal movements tend to be less variable and less intense. The detailed mapping of these horizontal velocities provides a better understanding of the spatial relationship between vertical and horizontal subsidence, which is crucial in evaluating the broader geodynamic processes affecting the Emilia-Romagna region.

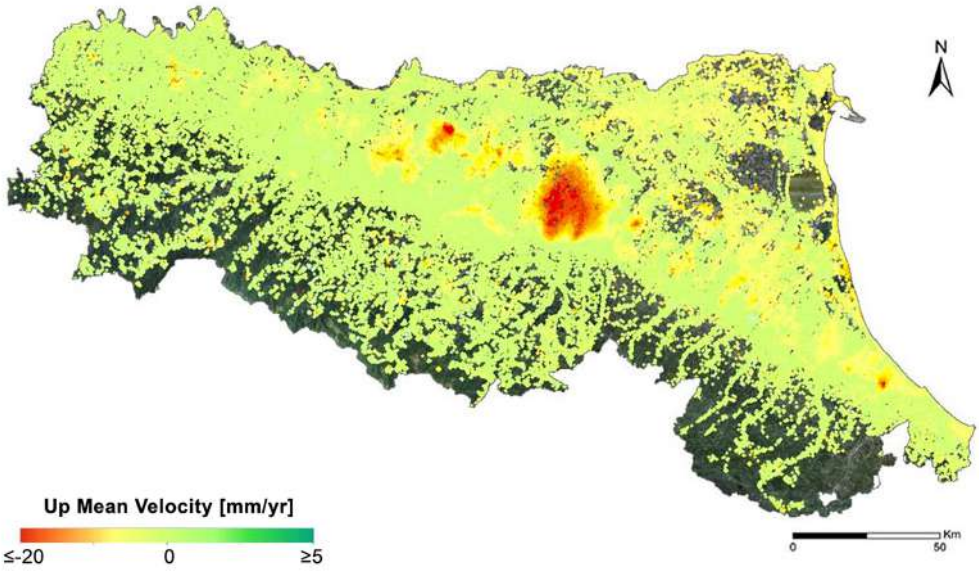

Figure 8. Mean up calibrated SqueeSAR® velocity [mm/yr] obtained for the 2016−2021 time span.

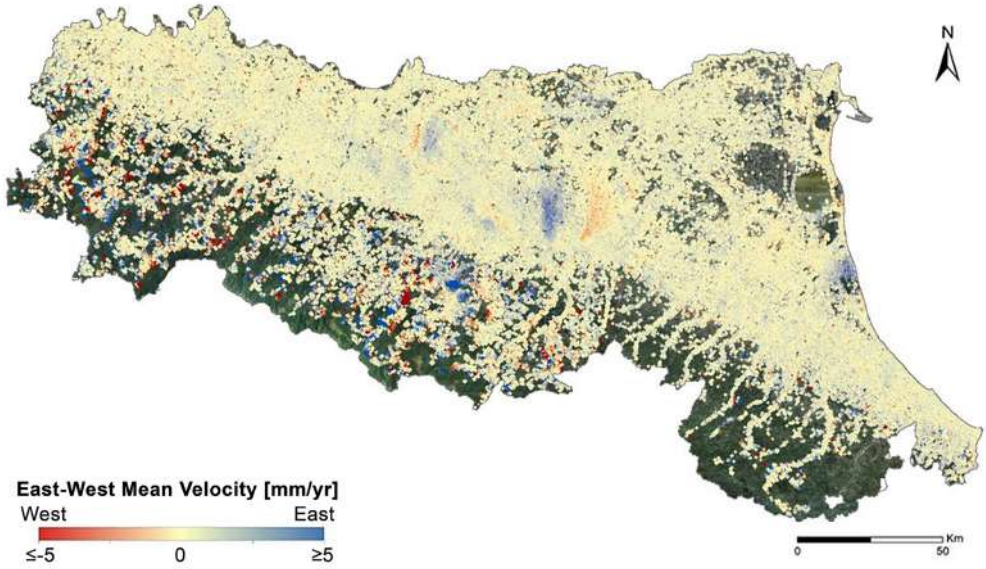

Figure 9. Mean east–west calibrated SqueeSAR® velocity [mm/yr] obtained for the 2016−2021 time span.

3.5. Outlier Rejection: Local Phenomena and Statistical Selection

The outlier rejection process aimed to identify and remove anomalous data points that could be the result of local anthropic activities or the structural subsidence of infrastructure. In this context, the term "outlier" refers to a pseudo-MP that shows little to no spatial correlation with surrounding measurement points. This lack of correlation suggests that the data do not reflect the regional subsidence phenomenon but may instead be caused by local factors, such as thermal deformation, structural movements, or issues with the interferometric method itself. These anomalies may also arise from urbanization or anthropogenic land management activities that interfere with the measurements. Given the large volume of data, the verification and validation of pseudo-MP is a critical and complex task that requires the use of objective statistical methods. However, these methods need to be complemented by visual assessments and specific evaluations conducted by the operator. The combination of statistical tools and expert judgment ensures that only valid measurements are retained, allowing for a more accurate interpretation of the subsidence data and the production of reliable maps and models. To ensure the accuracy of the displacement

data, two distinct verification procedures were employed to identify and remove outliers from the dataset.

- Initial Identification of Outliers. The first step involved analyzing the frequency distribution of the mean vertical velocities over the period of observation. This allowed for the detection of data points that were significantly outside the expected range. The identified outliers were primarily points with vertical velocities of less than −20.0 mm/year or greater than 5.0 mm/year. These values were then compared with known references and cross-checked with available land use and territorial context data.
- Automated and Statistical Selection of Outliers. Following the initial identification, an automated statistical procedure was applied to further refine the selection of outliers. This method helped to confirm and enhance the accuracy of the data by eliminating those measurement points that deviated from the general pattern of subsidence in the region.

As a result of these procedures, 145 pseudo-MP were removed from the dataset. These outliers were primarily located in the lowland areas. After exclusion, the remaining data better represented the regional subsidence phenomenon, free from the influence of localized anthropic activities or infrastructure changes. The removed outliers were associated with areas where local factors, such as urbanization, infrastructure development, quarries, landfills, or new construction projects (like roads, overpasses, or photovoltaic systems), caused anomalous displacement velocities. The exclusion of these outliers helps to ensure that the resulting subsidence map accurately reflects natural ground motion without interference from human activities. Figures 10 and 11 illustrate the locations of these identified outliers and show examples at the local scale, highlighting how the velocities of the anomalous points deviate significantly from the surrounding values. This further emphasizes the role of human activity and infrastructure in producing these unusual measurements.

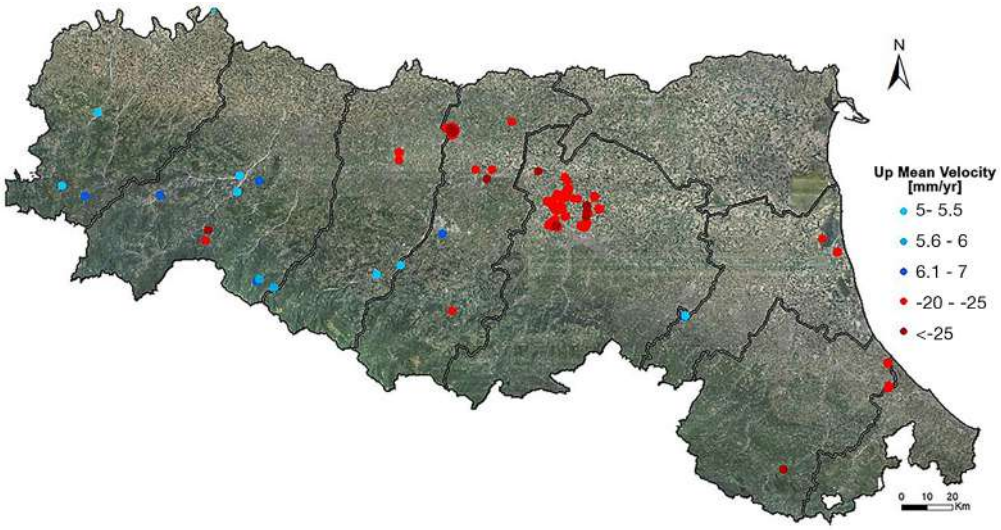

Figure 10. The location of outliers initially identified between the extremes (minima and maxima) of the frequency distribution of the period−averaged vertical velocities was compared with known anthropogenic activities in the area or highlighted individually by the mean velocity value.

Figure 11. Examples of areas exhibiting anomalous vertical ground velocities resulting from anthropogenic activities or infrastructure are identified as outliers. On the (**left**), a landfill; in the (**center**), a photovoltaic solar park; and on the (**right**), a viaduct.

The further automated and statistical selection of outliers involved applying an automatic procedure to the entire calibrated dataset of vertical velocities, which had also been used in the previous 2011–2016 survey. This allowed for the comparison of the vertical displacement velocity with the mean velocity of surrounding measurement points. The analysis was conducted using Kriging, where the variogram of the calibrated average vertical velocity data was used to determine the difference between the values of individual measurement points and the corresponding values from the spatial analysis. This process led to the identification of deviations between the measured values and the expected values, which should ideally be zero to confirm the assumption of stationarity necessary for Kriging analysis. The capture radius was defined according to the variogram model, aligned with the goal of local outlier detection. In areas with low point densities, where the minimum requirements could not be met, the algorithm increased the capture radius locally, assigning greater weight to the closer points compared to the more distant ones. The dataset was then cleaned of identified outliers through a recursive analysis process, with the modeled dataset continuously moving closer to the measured data. This iterative process ensured the production of a better-quality final map. A total of 942 potential outliers were identified within the entire dataset of 704,444 pseudo-MP, which included both lowland and hilly/mountain regions. Of these, all 145 initially identified outliers were confirmed. After removing these outliers, the dataset corresponding to the plain zone was confined to a polygon bounded by the regional boundary to the north, the coastline to the east, and the 100 m elevation contour. Additionally, a 1000 m planimetric buffer was applied to avoid edge effects in subsequent processing. This resulted in a final dataset consisting of 552,581 points.

3.6. The 2016–2021 Emilia-Romagna Subsidence Map

Based on the findings from previous periodic monitoring activities of vertical soil movements and the assessment of the subsidence phenomenon on a regional scale, a map of vertical soil movements for the period 2016–2021 was created. This map includes isokinetic curves with an interval of 2.5 mm/year, specifically for the regional lowland area. The area covered by this map is approximately 10,897 km^2. The following procedure was employed.

- The final dataset of the calibrated interferometric analysis 2016–2021 was used, cropped according to the regional boundary and the 100 m elevation line, with a buffer of 1 km to remove edge effects and outliers, for a total of 552,581 pseudo-MP.
- The spatialization of the data was carried out using the Kriging technique, generating a grid with a mesh size of 100 m × 100 m, co-registered with the grids calculated in the previous monitoring periods, in order to facilitate the comparison of the results in the GIS environment.
- The areas occupied by transitional surface waters, such as the Comacchio Valleys, were excluded from the calculated grid and thus from the final cartography.

- The final cartography was provided via the contour process in a GIS environment, giving isokinetic curves with a step of 2.5 mm/year.

The Emilia-Romagna subsidence map is presented in Figure 12.

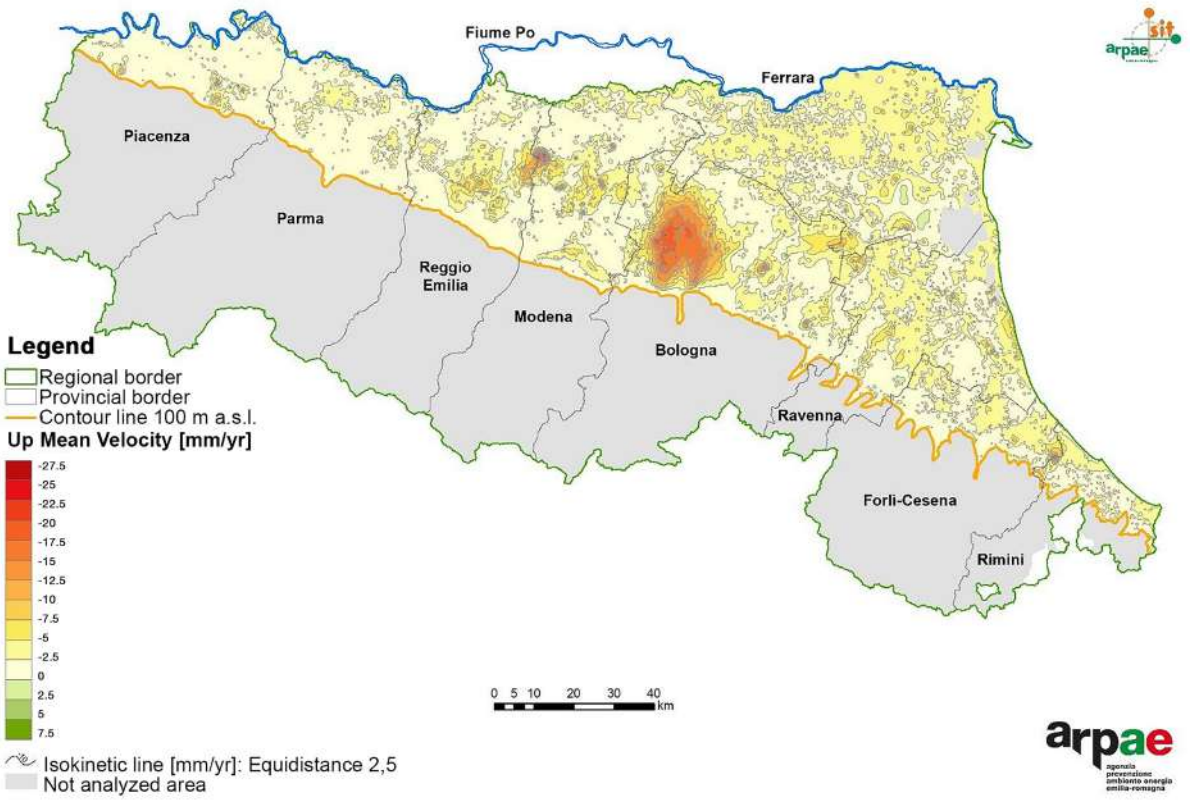

Figure 12. Map of vertical ground motion velocities for the period 2016−2021.

4. Discussion

The cartography of vertical soil movement in the Emilia-Romagna plains for the period 2016–2021 (Figure 12) highlights limited areas of uplift (green), extensive zones with velocities close to zero (white), and regions affected by soil lowering—both natural and anthropogenic subsidence—primarily north of Bologna and in other localized areas (orange and red). Natural subsidence results from sediment compression and the loss of interstitial fluids due to overburden pressure, natural compaction, and tectonic activity. In contrast, anthropogenic subsidence is mainly driven by groundwater extraction, which induces sediment compaction [67]. During the 2016–2021 period, the mean vertical soil velocity in the lowland area ranged between 0 and −5 mm/year across 89.6% of the territory. Meanwhile, 6.1% of the area exhibited velocities between −5 and −10 mm/year, while 2.9% recorded velocities below -10 mm/year. The highest subsidence rates were observed in the province of Modena, followed by Bologna, which also displayed the greatest variability at the regional scale. The overall frequency distribution of the movement velocities for this period ranged from 5.15 mm/year to −27.29 mm/year, with a median value of −2.37 mm/year.

To better characterize the subsidence phenomena in the Emilia-Romagna region, a comparison of the vertical soil velocities from the 2016–2021 period with those from 2011–2016 and 2006–2011 has been conducted, and the frequency distribution of each period is reported in Figure 13 and Table 5. This analysis provides insights into temporal variations and trends, allowing for a more comprehensive understanding of the evolution of subsidence across the region.

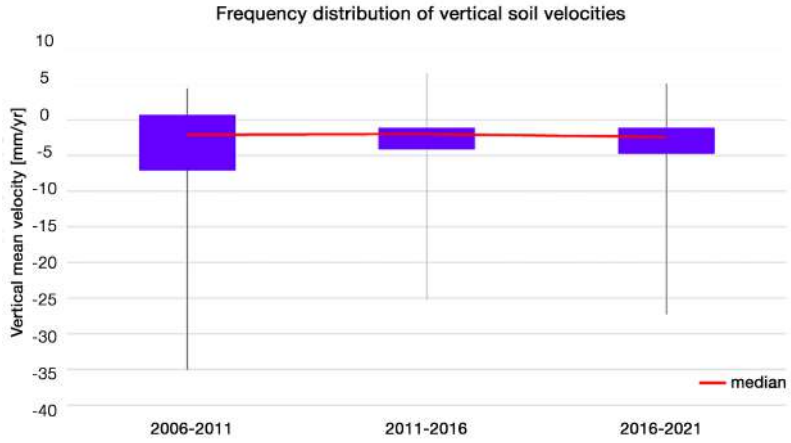

Figure 13. Frequency distribution of vertical soil velocities from 2006 to 2021 for each analyzed period (2006−2011, 2011−2016, 2016−2021). The distribution shows the range of velocities for each period (grey line), from extreme subsidence to uplift, the values between the 10th and 90th percentiles (purple box), and the median values (red line), providing insights into temporal changes in the soil movement dynamics over time.

Table 5. Values of the frequency distribution of the vertical soil velocities from 2006 to 2021 for each analyzed period (2006–2011, 2011–2016, 2016–2021) as reported in Figure 13, expressed in [mm/yr].

	Maximum	10° Percentile	Median	90° Percentile	Minimum
2006–2011	4.42	0.70	−2.00	−7.08	−35.05
2011–2016	6.63	−1.13	−1.93	−4.05	−25.24
2016–2021	5.15	−1.13	−2.37	−4.75	−27.29

A comparison of the minimum velocity values with those from the 2006–2011 period reveals that they are generally comparable, although slightly lower, as the subsidence values in the earlier period reached −35.05 mm/year. The median velocity values for the most recent period (2016–2021) are marginally lower at the regional scale compared to previous periods (Figure 13 and Table 5). Additionally, when comparing the movement velocities between the 2016–2021 and 2011–2016 periods, it is observed that 85.47% of the plain territory does not exhibit significant changes in trend. However, 11.17% of the area has experienced an increase in subsidence, while 3.36% of the surface has shown a reduction in subsidence.

To further analyze the evolution of subsidence between 2006 and 2021 in the Emilia-Romagna region, Figure 14 illustrates the vertical soil variations for the periods 2006–2011 to 2011–2016 and 2011–2016 to 2016–2021 [68]. This comparison highlights the temporal changes in the subsidence and uplift patterns across the region, offering a detailed view of the shifting dynamics of vertical soil movement over time. For both maps in Figure 14, the reference period is the older one (2006–2011 for Figure 14A, 2011–2016 for Figure 14B).

Specifically, considering Figure 14B, at the provincial scale, the provinces of Piacenza, Parma, and Reggio Emilia exhibit widespread negative variation (yellow areas), whereas, in previous periods, they had consistently shown average trends toward a rising topographic surface (yellow areas in Figure 14A). Furthermore, in the province of Bologna, a large area north of the city exhibits negative variation (orange areas), while, to the east, some localized areas display signs of improvement (green areas), whereas others indicate a worsening trend (yellow areas). The plain area north of Bologna, historically characterized by high subsidence rates, had shown a progressive reduction in the previous monitoring period (2006–2016), as shown in Figure 14A, where the subsidence had significantly decreased (green areas), with some areas even recording positive velocities (uplift) [69]. This de-

cline was primarily attributed to reduced groundwater extraction and favorable climatic conditions during that period. However, Figure 14B, which covers the 2011–2021 period, indicates the resurgence of subsidence across this historically critical area (orange areas), although at lower rates than in the past. Modena and Ferrara also show some areas of improvement (green areas) compared with the period 2006–2016, while Ravenna presents the most extensive zones of positive variation, even along the coast (green areas), with only limited and fragmented areas of worsening (yellow areas). Finally, at the border between Cesena and Rimini, a worsening trend is evident (yellow areas) compared to the period of 2006–2016 (yellow areas in Figure 14A). Future studies will focus on further investigating soil movement at the provincial level, correlating the vertical variation data with groundwater levels, groundwater abstraction, and precipitation. This approach will help to identify the specific causes and local dynamics behind the subsidence phenomena, enhance our understanding of the interactions between natural and anthropogenic factors, and contribute to more targeted and effective management strategies.

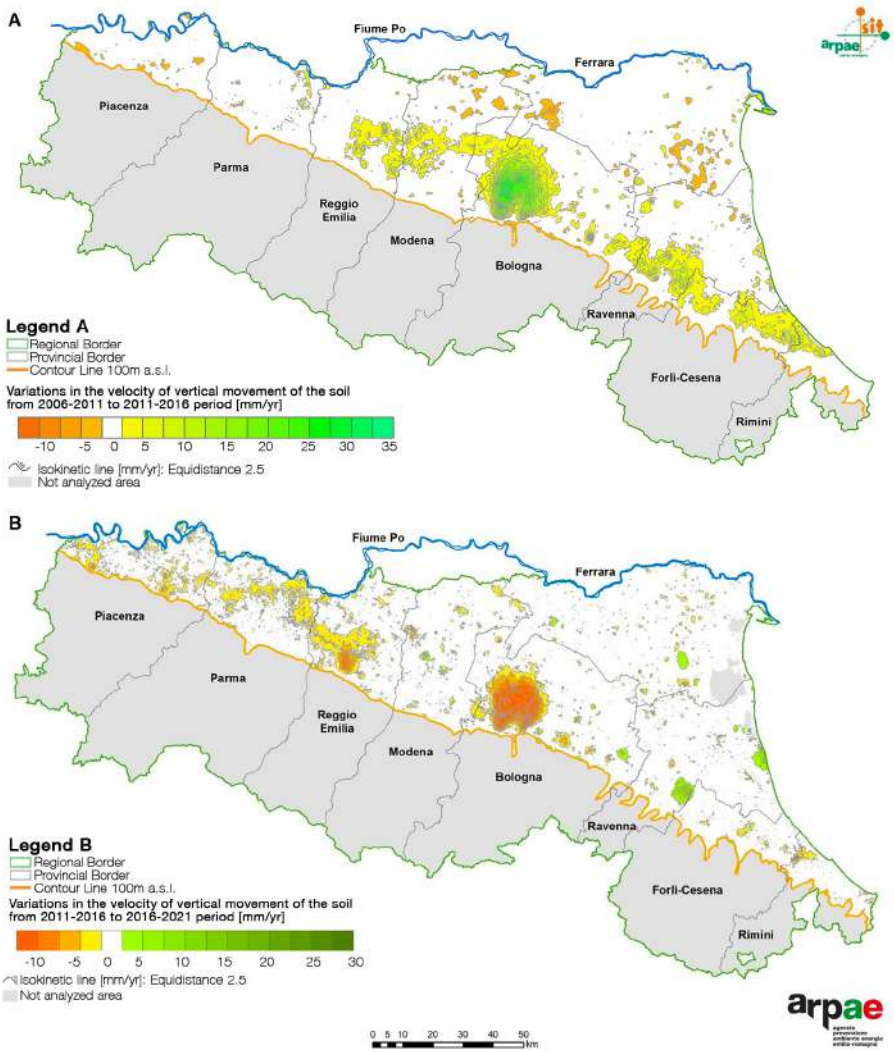

Figure 14. Maps of the variations in the vertical movement velocities of the ground from the period 2006−2011 to the period 2011−2016 (**A**) and from the period 2011–2016 to the period 2016–2021 (**B**).

5. Conclusions

The most recent map of vertical soil movement for the period 2016–2021, developed through the integration of ascending and descending InSAR data, represents a groundbreaking achievement as the first ever subsidence map for the Emilia-Romagna region created

using this advanced approach. This advancement significantly improves the monitoring of subsidence by providing a more accurate, high-resolution, and comprehensive representation of the phenomenon across the region. The combination of these two InSAR geometries allows for the detection and analysis of vertical displacements with unprecedented spatial precision, reducing uncertainties and enabling the more detailed interpretation of subsidence patterns. Furthermore, the processing of GNSS data using specialized software for precise point positioning (PPP) played a crucial role in calibrating the InSAR dataset. This step ensures the accurate alignment of satellite-derived measurements with a well-established and dense geodetic reference frame, enhancing the reliability and consistency of the data. The integration of GNSS and InSAR technologies has thus led to a refined dataset that minimizes systematic errors and provides a robust basis for long-term monitoring and trend analysis. This updated map is pivotal in assessing how the subsidence patterns have evolved since the 2011–2016 period, offering critical insights into ongoing shifts and emerging trends. Compared to previous analyses, it reveals not only areas of continued subsidence but also potential changes in intensity and spatial distribution. The ability to detect even subtle variations in ground deformation is essential in evaluating the underlying causes, which may be linked to natural geological processes, anthropogenic activities, or variations in groundwater extraction. The significance of this work extends beyond scientific research, as it has direct implications for urban planning, infrastructure maintenance, and risk management. The integration of advanced InSAR and GNSS techniques provides regional authorities and stakeholders with the most precise and up-to-date information available, enabling them to implement informed mitigation strategies and policy decisions. This is particularly important in a region like Emilia-Romagna, where subsidence can impact critical infrastructure, water management systems, and land stability. In conclusion, this study underscores the dynamic nature of subsidence and highlights the need for continuous monitoring using state-of-the-art geodetic techniques. The evolution of remote sensing methodologies, combined with rigorous data processing and validation, has allowed for a more refined understanding of the phenomenon. Looking ahead, further advancements in satellite technologies, data fusion techniques, and machine learning applications will continue to improve our ability to monitor and predict subsidence with even greater accuracy. By maintaining a proactive approach to monitoring, Emilia-Romagna can better anticipate and mitigate the effects of subsidence, ensuring the resilience and sustainability of its territory for future generations.

Author Contributions: Conceptualization, G.B., E.G., A.L., M.M. (Marco Marcaccio), M.M. (Marianna Mazzei) and L.V.; methodology, G.B., A.F., C.G., E.G., A.L. and L.V.; validation, G.B., E.G., A.L. and L.V.; formal analysis, G.B., A.F., C.G., E.G., A.L., M.M. (Marco Marcaccio), M.M. (Marianna Mazzei) and L.V.; investigation, G.B., A.F., C.G., E.G., A.L., M.M. (Marco Marcaccio), M.M. (Marianna Mazzei) and L.V.; resources, G.B., A.F., C.G., E.G., A.L. and L.V.; writing—original draft preparation, E.G.; writing—review and editing, G.B., A.F., C.G., E.G., A.L., M.M. (Marco Marcaccio), M.M. (Marianna Mazzei) and L.V.; visualization, E.G., M.M. (Marianna Mazzei) and C.G.; supervision, G.B., A.F., M.M. (Marco Marcaccio) and L.V.; project administration, G.B., M.M. (Marco Marcaccio) and L.V.; funding acquisition, M.M. (Marco Marcaccio). All authors have read and agreed to the published version of the manuscript.

Funding: The regional campaigns for subsidence monitoring have been financed by the Emilia-Romagna region.

Data Availability Statement: The data presented in this study were derived from the following resources available in the public domain: Copernicus https://asf.alaska.edu, (accessed on 10 January 2022); EUREF https://www.epncb.oma.be, (accessed on 10 January 2022).

Acknowledgments: We would like to express our gratitude to Monica Carati (Arpae, Direzione Tecnica) for cartography and GIS processing, and to Andrea Chahoud and Paolo Spezzani (Centro Tematico Regionale Sistemi Idrici-Direzione Tecnica Arpae) for providing data and assessments on groundwater abstraction. We also thank Luisa Perini and Paolo Severi (Area Geologia, Suoli e Sismica-Settore Difesa del Territorio-Regione Emilia-Romagna) and Giacomo Zaccanti (Servizio Osservatorio Energia Rifiuti e Siti Contaminati-Direzione Tecnica Arpae) for sharing monitoring data and contributing to the continuous methodological discussions. Their support and collaboration have been invaluable to this study.

Conflicts of Interest: The authors declare no conflicts of interest.

Appendix A

The locations of the 28 GNSS stations exploited in the present study to calibrate the InSAR data and validate the calibration process are reported in Table A1.

Table A1. Geographical coordinates of the GNSS permanent stations selected for the calibration and validation phase of the InSAR data.

Marker	Longitude	Latitude
Calibration		
BGDR	43.8891	11.8950
BLGN	44.5110	11.3506
BOBB	44.7706	9.3834
BRAS	44.1222	11.1131
BRIS	44.2248	11.7660
CAST	44.4316	10.4053
CODI	44.8367	12.1120
FERR	44.8279	11.6013
GARI	44.6769	12.2494
GUAS	44.9178	10.6623
ITIM	44.3475	11.7179
MODE	44.6289	10.9487
MSEL	44.5200	11.6465
MTRZ	44.3128	11.4250
PARM	44.7646	10.3122
PIAC	45.0431	9.6897
RAVE	44.4053	12.1919
REGG	44.7064	10.6368
SGIP	44.6355	11.1827
TARO	44.4879	9.7657
VERG	44.2874	11.1105
Validation		
BOL1	44.4876	11.3288
BOLG	44.5002	11.3568
COLL	44.7528	10.2160
XXX1	44.4000	12.3000
ITRN	44.0483	12.5821
MOPS	44.6294	10.9492
XXX2	44.6000	12.3000

Appendix B

Tables A2 and A3 provide a summary of the calibration reference values for the vertical and east–west components, respectively. In detail, in both tables, for the up and east velocity components, we report

- the mean velocity of the filtered GNSS data;
- the mean velocity of the selected radar targets around the GNSS station;
- the number of radar targets selected for the calculation of the average speed;
- the relative standard deviation of the average speeds of the selected radar targets;
- the differences used for plan estimation and removal.

The average difference time series and the average residual time series, obtained from the comparison between the GNSS time series and the averaged MP ones, are reported

in Figures A1 and A2. These time series represent the movement of the local SqueeSAR® reference point relative to the absolute GNSS network. These time series were then removed from the time series of all SqueeSAR® points, obtaining the calibrated SqueeSAR® data, constrained to the same GNSS network reference system.

Table A2. Calibration reference values for the up component. In the table, we report the station number, station marker, up GNSS velocity [mm/yr], up SqueeSAR® velocity [mm/yr], SqueeSAR® standard deviation of the velocity [mm/yr], number of SqueeSAR® MP associated with each GNSS station, and velocity difference between the SqueeSAR® and GNSS up velocities.

Marker	V_U GNSS [mm/yr]	V_U SqueeSAR® [mm/yr]	œ V_U SqueeSAR® [mm/yr]	SqueeSAR® n° MP	ΔV_E [mm/yr]
BGDR	0.9	-	-	0	-
BLGN	−8.3	−5.5	0.3	5	2.8
BOBB	−0.6	1.1	0.5	5	1.7
BRAS	0.5	0.4	0	1	−0.1
BRIS	0.6	-	-	0	-
CAST	0.8	0.7	0.2	5	−0.1
CODI	−2.8	−0.1	0.4	5	2.7
FERR	−1	0.2	0.3	5	1.3
GARI	−2.8	0	0.4	5	2.8
GUAS	−1.6	0.3	0.3	5	2
ITIM	−0.4	0.7	0.2	5	1.1
MODE	−4.4	−0.7	0.2	5	3.8
MSEL	−1.9	1.9	0.5	2	3.8
MTRZ	0	-	-	0	-
PARM	−0.1	0.9	0.8	5	1
PIAC	−0.7	0.2	0.2	5	0.9
RAVE	−3.8	−0.6	0.4	5	3.2
REGG	−3.2	−0.1	0.2	5	3.1
SGIP	−7	−3.5	0.9	5	3.5
TARO	−0.6	0.2	0.1	5	0.8
VERG	0.7	1	0.1	5	0.2

Table A3. Calibration reference values for the east component. In the table, we report the station number, station marker, up GNSS velocity [mm/yr], east SqueeSAR® velocity [mm/yr], SqueeSAR® standard deviation of the velocity [mm/yr], number of SqueeSAR® MP associated with each GNSS station, and velocity difference between the SqueeSAR® and GNSS east velocities.

Marker	V_E GNSS [mm/yr]	V_E SqueeSAR® [mm/yr]	œ V_E SqueeSAR® [mm/yr]	SqueeSAR® n° MP	Δ V_E [mm/yr]
BGDR	0.2	-	-	0	-
BLGN	−0.9	−1.8	0.3	5	−0.9
BOBB	0.3	0.2	0.2	5	−0.2
BRAS	0	−0.1	0	1	−0.2
BRIS	1.1	-	-	0	-
CAST	0	−0.5	0.6	5	−0.5
CODI	0	−0.3	0.6	5	−0.3
FERR	0.4	0	0.2	5	−0.3
GARI	−0.3	−0.3	0.3	5	0
GUAS	0.1	−0.1	0.1	5	−0.3
ITIM	0.8	−0.2	0.2	5	−1
MODE	0.8	−0.1	0.1	5	−0.9
MSEL	0.9	0.6	0	2	−0.3
MTRZ	1.5	-	-	0	-
PARM	0.8	0.2	0.4	5	−0.6
PIAC	0.1	−0.1	0.1	5	−0.3
RAVE	0.3	0	0.6	5	−0.3
REGG	−0.2	0.3	0.2	5	0.5
SGIP	1.5	1.4	1.1	5	−0.1
TARO	0.2	0.1	0.2	5	−0.1
VERG	1.8	0.5	0.2	5	−1.3

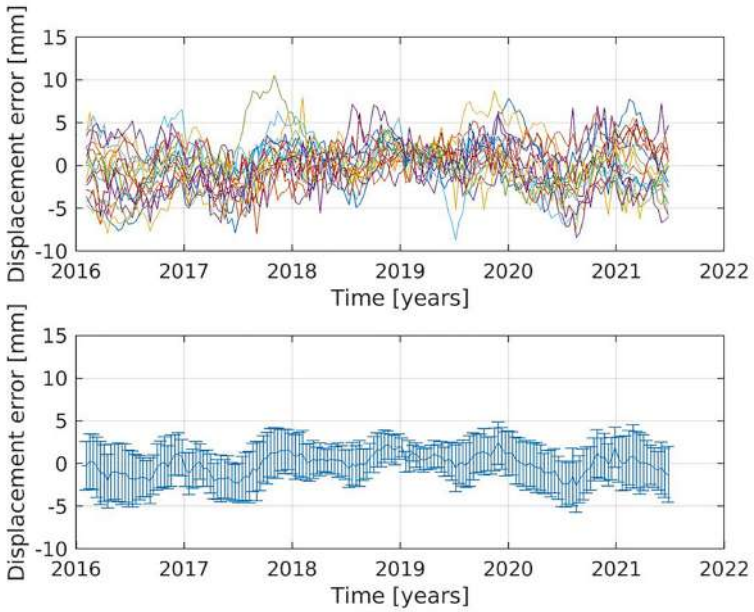

Figure A1. The time series of the residuals between the averaged MP time series and the GNSS ones in the up component (**above**). The average unique common time series of the residuals (cRTS) in the up (vertical) direction (**below**).

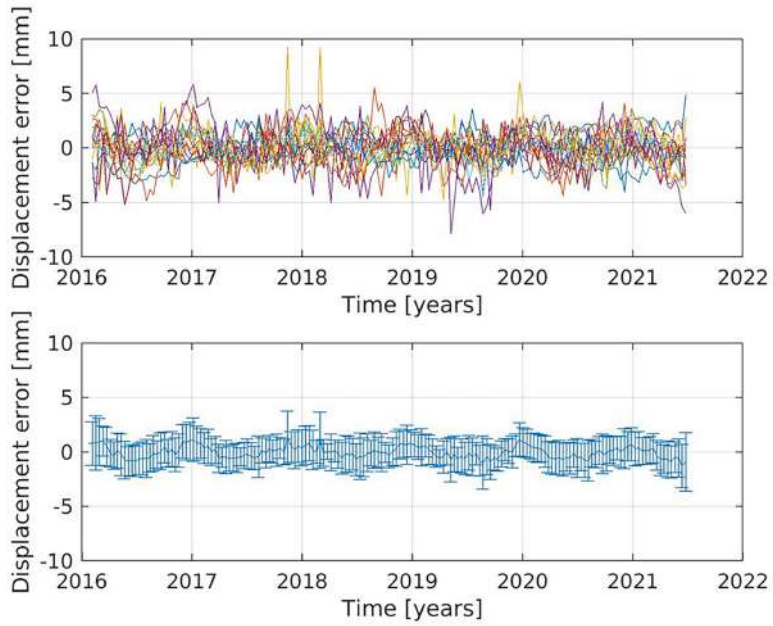

Figure A2. The time series of the residuals between the averaged MP time series and the GNSS ones in the east component (**above**). The average unique common time series of the residuals (cRTS) in the east direction (**below**).

References

1. Loupasakis, C.; Rozos, D. Finite-Element Simulation of Land Subsidence Induced by Water Pumping in Kalochori Village, Greece. *Q. J. Eng. Geol. Hydrogeol.* **2009**, *42*, 369–382. [CrossRef]
2. Galloway, D.L.; Burbey, T.J. Review: Regional Land Subsidence Accompanying Groundwater Extraction. *Hydrogeol. J.* **2011**, *19*, 1459–1486. [CrossRef]
3. Herrera-García, G.; Ezquerro, P.; Tomás, R.; Béjar-Pizarro, M.; López-Vinielles, J.; Rossi, M.; Mateos, R.M.; Carreón-Freyre, D.; Lambert, J.; Teatini, P.; et al. Mapping the Global Threat of Land Subsidence. *Science* **2021**, *371*, 34–36. [CrossRef] [PubMed]
4. Candela, T.; Koster, K. The Many Faces of Anthropogenic Subsidence. *Science* **2022**, *376*, 1381–1382. [CrossRef] [PubMed]
5. Tzampoglou, P.; Ilia, I.; Karalis, K.; Tsangaratos, P.; Zhao, X.; Chen, W. Selected Worldwide Cases of Land Subsidence Due to Groundwater Withdrawal. *Water* **2023**, *15*, 1094. [CrossRef]

6. Bagheri-Gavkosh, M.; Hosseini, S.M.; Ataie-Ashtiani, B.; Sohani, Y.; Ebrahimian, H.; Morovat, F.; Ashrafi, S. Land Subsidence: A Global Challenge. *Sci. Total Environ.* **2021**, *778*, 146193. [CrossRef]
7. Ohenhen, L.O.; Shirzaei, M.; Barnard, P.L. Slowly but Surely: Exposure of Communities and Infrastructure to Subsidence on the US East Coast. *PNAS Nexus* **2023**, *3*, pgad426. [CrossRef]
8. Huning, L.S.; Love, C.A.; Anjileli, H.; Vahedifard, F.; Zhao, Y.; Chaffe, P.L.B.; Cooper, K.; Alborzi, A.; Pleitez, E.; Martinez, A.; et al. Global Land Subsidence: Impact of Climate Extremes and Human Activities. *Rev. Geophys.* **2024**, *62*, e2023RG000817. [CrossRef]
9. Xu, Y.; Wu, Z.; Zhang, H.; Liu, J.; Jing, Z. Land Subsidence Monitoring and Building Risk Assessment Using InSAR and Machine Learning in a Loess Plateau City—A Case Study of Lanzhou, China. *Remote Sens.* **2023**, *15*, 2851. [CrossRef]
10. Jin, B.; Zeng, T.; Wang, T.; Zhang, Z.; Gui, L.; Yin, K.; Zhao, B. Advanced Risk Assessment Framework for Land Subsidence Impacts on Transmission Towers in Salt Lake Region. *Environ. Model. Softw.* **2024**, *177*, 106058. [CrossRef]
11. He, Y.; Li, X.; Yang, J.; Liu, Y.; Yang, G.; Hu, M.; Chen, S.; Yao, H.; Wang, L.; Xiong, X. Urban Land Subsidence Monitoring and Risk Assessment Using the Point Target Based SBAS-InSAR Method: A Case Study of Changsha City. *Remote Sens. Lett.* **2024**, *15*, 689–699. [CrossRef]
12. Brandt, J.T.; Sneed, M.; Danskin, W.R. Detection and Measurement of Land Subsidence and Uplift Using Interferometric Synthetic Aperture Radar, San Diego, California, USA, 2016–2018. *Proc. Int. Assoc. Hydrol. Sci.* **2020**, *382*, 45–49. [CrossRef]
13. Zhu, Z.; Qiu, S.; Ye, S. Remote Rensing of Land Change: A MUltifaceted Perspective. *Remote Sens. Environ.* **2022**, *282*, 113266. [CrossRef]
14. Ghorbani, Z.; Khosravi, A.; Maghsoudi, Y.; Mojtahedi, F.F.; Javadnia, E.; Nazari, A. Use of InSAR Data for Measuring Land Subsidence Induced by Groundwater Withdrawal and Climate Change in Ardabil Plain, Iran. *Sci. Rep.* **2022**, *12*, 13998. [CrossRef]
15. Dacome, M.C.; Miandro, R.; Vettorel, M.; Roncari, G. Subsidence Monitoring Network: An Italian Example Aimed at a Sustainable Hydrocarbon E&P Activity. *Proc. Int. Assoc. Hydrol. Sci.* **2015**, *372*, 379–384. [CrossRef]
16. Teatini, P.; Ferronato, M.; Gambolati, G.; Bertoni, W.; Gonella, M. A Century of Land Subsidence in Ravenna, Italy. *Environ. Geol.* **2005**, *47*, 831–846. [CrossRef]
17. Demoulin, A.; Collignon, A. Nature of the Recent Vertical Ground Movements Inferred from High-Precision Leveling Data in an Intraplate Setting: NE Ardenne, Belgium. *J. Geophys. Res. Solid Earth* **2000**, *105*, 693–705. [CrossRef]
18. Gleason, S. *GNSS Applications and Methods*, 1st ed.; Artech House: Norwood, MA, USA, 2009.
19. Petropoulos, G.P.; Srivastava, P.K. (Eds.) *GPS and GNSS Technology in Geosciences*; Elsevier: Amsterdam, The Netherlands; Oxford, UK; Cambridge, MA, USA, 2021.
20. Tao, Q.; Li, X.; Gao, T.; Chen, Y.; Liu, R.; Xiao, Y. Land Subsidence Monitoring and Analysis in Qingdao, China Using Time Series InSAR Combining PS and DS. *Geomat. Nat. Hazards Risk* **2025**, *16*, 2447543. [CrossRef]
21. Navarro-Hernández, M.I.; Tomás, R.; Valdes-Abellan, J.; Bru, G.; Ezquerro, P.; Guardiola-Albert, C.; Elçi, A.; Batkan, E.A.; Caylak, B.; Ören, A.H.; et al. Monitoring land subsidence Induced by Tectonic Activity and Groundwater Extraction in the Eastern Gediz River Basin (Türkiye) Using Sentinel-1 Observations. *Eng. Geol.* **2023**, *327*, 107343. [CrossRef]
22. Giorgini, E.; Vecchi, E.; Poluzzi, L.; Tavasci, L.; Barbarella, M.; Gandolfi, S. 15 years of the Italian GNSS Geodetic Reference Frame (RDN): Preliminary analysis and considerations. In *Geomatics for Green and Digital Transition*; Borgogno-Mondino, E., Zamperlin, P., Eds.; Springer International Publishing: Cham, Switzerland, 2022; Volume 1651, pp. 3–14. [CrossRef]
23. Parizzi, A.; Rodriguez Gonzalez, F.; Brcic, R. A Covariance-Based Approach to Merging InSAR and GNSS Displacement Rate Measurements. *Remote Sens.* **2020**, *12*, 300. [CrossRef]
24. Ferretti, A.; Fumagalli, A.; Passera, E.; Rucci, A. Insar Data Calibration in Wide Area Processing. In Proceedings of the IGARSS 2022—2022 IEEE International Geoscience and Remote Sensing Symposium, Kuala Lumpur, Malaysia, 17–22 July 2022; pp. 5101–5104. [CrossRef]
25. Hanssen, R.F. *Radar Interferometry Data Interpretation and Error Analysis*; Remote Sensing and Digital Image Processing; Springer: Dordrecht, The Netherlands, 2001; Volume 2. [CrossRef]
26. Watson, A.R.; Elliott, J.R.; Lazecký, M.; Maghsoudi, Y.; McGrath, J.D.; Walters, R.J. An InSAR-GNSS Velocity Field for Iran. *Geophys. Res. Lett.* **2024**, *51*, e2024GL108440. [CrossRef]
27. Hussain, E.; Wright, T.J.; Walters, R.J.; Bekaert, D.; Hooper, A.; Houseman, G.A. Geodetic Observations of Postseismic Creep in the Decade After the 1999 Izmit Earthquake, Turkey: Implications for a Shallow Slip Deficit. *J. Geophys. Res. Solid Earth* **2016**, *121*, 2980–3001. [CrossRef]
28. Weiss, J.R.; Walters, R.J.; Morishita, Y.; Wright, T.J.; Lazecky, M.; Wang, H.; Hussain, E.; Hooper, A.J.; Elliott, J.R.; Rollins, C.; et al. High-Resolution Surface Velocities and Strain for Anatolia From Sentinel-1 InSAR and GNSS Data. *Geophys. Res. Lett.* **2020**, *47*, e2020GL087376. [CrossRef]
29. Raspini, F.; Caleca, F.; Del Soldato, M.; Festa, D.; Confuorto, P.; Bianchini, S. Review of Satellite Radar Interferometry for Subsidence Analysis. *Earth-Sci. Rev.* **2022**, *235*, 104239. [CrossRef]
30. Fabris, M.; Battaglia, M.; Chen, X.; Menin, A.; Monego, M.; Floris, M. An Integrated InSAR and GNSS Approach to Monitor Land Subsidence in the Po River Delta (Italy). *Remote Sens.* **2022**, *14*, 5578. [CrossRef]

31. Costantini, M.; Ferretti, A.; Minati, F.; Falco, S.; Trillo, F.; Colombo, D.; Novali, F.; Malvarosa, F.; Mammone, C.; Vecchioli, F.; et al. Analysis of Surface Deformations Over the Whole Italian Territory by Interferometric Processing of ERS, Envisat and COSMO-SkyMed radar data. *Remote Sens. Environ.* **2017**, *202*, 250–275. [CrossRef]
32. Giorgini, E.; Orellana, F.; Arratia, C.; Tavasci, L.; Montalva, G.; Moreno, M.; Gandolfi, S. InSAR Monitoring Using Persistent Scatterer Interferometry (PSI) and Small Baseline Subset (SBAS) Techniques for Ground Deformation Measurement in Metropolitan Area of Concepción, Chile. *Remote Sens.* **2023**, *15*, 5700. [CrossRef]
33. Chen, D.; Wu, Q.; Sun, Z.; Shi, X.; Zhang, S.; Zhang, Y.; Wu, Y. Semi-Automatic Detection of Ground Displacement from Multi-Temporal Sentinel-1 Synthetic Aperture Radar Interferometry Analysis and Density-Based Spatial Clustering of Applications with Noise in Xining City, China. *Remote Sens.* **2024**, *16*, 3066.
34. Livani, M.; Petracchini, L.; Benetatos, C.; Marzano, F.; Billi, A.; Carminati, E.; Doglioni, C.; Petricca, P.; Maffucci, R.; Codegone, G.; et al. Subsurface Geological and Geophysical Data from the Po Plain and the Northern Adriatic Sea (north Italy). *Earth Syst. Sci. Data* **2023**, *15*, 4261–4293. [CrossRef]
35. Severi, P. Soil Uplift in the Emilia-Romagna Plain (Italy) by Satellite Radar Interferometry. *Bull. Geophys. Oceanogr.* **2021**, *62*, 527–542. [CrossRef]
36. Margheriti, L.; Pondrelli, S.; Piccinini, D.; Agostinetti, N.P.; Giovani, L.; Salimbeni, S.; Lucente, F.P.; Amato, A.; Baccheschi, P.; Park, J. The Subduction Structure of the Northern Apennines: Results from the RETREAT Seismic Deployment. *Ann. Geophys.* **2009**, *49*, 1119–1131. [CrossRef]
37. Colantoni, P.; Gallignani, P.; Lenaz, R. Late Pleistocene and Holocene Evolution of the North Adriatic Continental Shelf (Italy). *Mar. Geol.* **1979**, *33*, M41–M50. [CrossRef]
38. Lucente, F.P.; Speranza, F. Belt Bending Driven by Lateral Bending of Subducting Lithospheric Slab: Geophysical Evidences from the Northern Apennines (Italy). *Tectonophysics* **2001**, *337*, 53–64. [CrossRef]
39. Speranza, F.; Sagnotti, L.; Mattei, M. Tectonics of the Umbria-Marche-Romagna Arc (central northern Apennines, Italy): New paleomagnetic constraints. *J. Geophys. Res. Solid Earth* **1997**, *102*, 3153–3166. [CrossRef]
40. Lucente, F.P.; Chiarabba, C.; Cimini, G.B.; Giardini, D. Tomographic Constraints on the Geodynamic Evolution of the Italian Region. *J. Geophys. Res. Solid Earth* **1999**, *104*, 20307–20327. [CrossRef]
41. Zuccarini, A.; Giacomelli, S.; Severi, P.; Berti, M. Long-Term Spatiotemporal Evolution of Land SUubsidence in the Urban Area of Bologna, Italy. *Bull. Eng. Geol. Environ.* **2024**, *83*, 35. [CrossRef]
42. Caputo, M.; Pieri, L.; Unguendoli, M. Geometric Investigation of the Subsidence in the Po Delta. In *Bollettino di Geofisica Teorica e Applicata*; IGM: Florence, Italy, 1970; Volume 13, pp. 187–207.
43. Donaldson, E.C.; Chilingarian, G.V.; Fu Yen, T. Chapter 1 Introduction to compaction/subsidence—Introduction to tectonics and sedimentation. In *Developments in Petroleum Science*; Elsevier: Amsterdam, The Netherlands, 1995; Volume 41, pp. 1–45. [CrossRef]
44. Eid, C.; Benetatos, C.; Rocca, V. Fluid Production Dataset for the Assessment of the Anthropogenic Subsidence in the Po Plain Area (Northern Italy). *Resources* **2022**, *11*, 53. [CrossRef]
45. Carbognin, L.; Tosi, L. Interaction between Climate Changes, Eustacy and Land Subsidence in the North Adriatic Region, Italy. *Mar. Ecol.* **2002**, *23*, 38–50. [CrossRef]
46. Gambolati, G. *Cenas Coastline Evolution of the Upper Adriatic Sea Due to Sea Level Rise and Natural and Anthropogenic Land Subsidence*; Number v.28 in Water Science and Technology Library; Springer: Dordrecht, The Netherlands, 1998.
47. Bitelli, G.; Bonsignore, F.; Pellegrino, I.; Vittuari, L. Evolution of the Techniques for Subsidence Monitoring at Regional Scale: The Case of Emilia-Romagna Region (Italy). *Proc. Int. Assoc. Hydrol. Sci.* **2015**, *372*, 315–321. [CrossRef]
48. Bitelli, G.; Bonsignore, F.; Unguendoli, M. Levelling and GPS Networks to Monitor Ground Subsidence in the Southern Po Valley. *J. Geodyn.* **2000**, *30*, 355–369. [CrossRef]
49. Bitelli, G.; Bonsignore, F.; Del Conte, S.; Franci, F.; Lambertini, A.; Novali, F.; Severi, P.; Vittuari, L. Updating the Subsidence Map of Emilia-Romagna Region (Italy) by Integration of SAR Interferometry and GNSS Time Series: The 2011–2016 Period. *Proc. Int. Assoc. Hydrol. Sci.* **2020**, *382*, 39–44. [CrossRef]
50. Panetti, A.; Rostan, F.; L'Abbate, M.; Bruno, C.; Bauleo, A.; Catalano, T.; Cotogni, M.; Galvagni, L.; Pietropaolo, A.; Taini, G.; et al. Copernicus Sentinel-1 Satellite and C-SAR instrument. In Proceedings of the 2014 IEEE Geoscience and Remote Sensing Symposium, Quebec City, QC, Canada, 13–18 July 2014; pp. 1461–1464. [CrossRef]
51. De Zan, F.; Monti Guarnieri, A. TOPSAR: Terrain Observation by Progressive Scans. *IEEE Trans. Geosci. Remote Sens.* **2006**, *44*, 2352–2360. [CrossRef]
52. Potin, P.; Rosich, B.; Miranda, N.; Grimont, P.; Shurmer, I.; O'Connell, A.; Krassenburg, M.; Gratadour, J.B. Copernicus Sentinel-1 Constellation Mission Operations Status. In Proceedings of the IGARSS 2019—2019 IEEE International Geoscience and Remote Sensing Symposium, Yokohama, Japan, 28 July–2 August 2019; pp. 5385–5388. [CrossRef]
53. Fuhrmann, T.; Garthwaite, M.C. Resolving Three-Dimensional Surface Motion with InSAR: Constraints from Multi-Geometry Data Fusion. *Remote Sens.* **2019**, *11*, 241. [CrossRef]

54. Grandin, R. Interferometric Processing of SLC Sentinel-1 TOPS Data. In Proceedings of the Fringe 2015: Advances in the Science and Applications of SAR Interferometry and Sentinel-1 InSAR Workshop, Frascati, Italy, 23–27 March 2015; European Space Agency: Frascati, Italy, 2015. [CrossRef]
55. Ferretti, A.; Fumagalli, A.; Novali, F.; Prati, C.; Rocca, F.; Rucci, A. A New Algorithm for Processing Interferometric Data-Stacks: SqueeSAR. *IEEE Trans. Geosci. Remote Sens.* **2011**, *49*, 3460–3470. [CrossRef]
56. Ferretti, A.; Prati, C.; Rocca, F. Permanent scatterers in SAR interferometry. *IEEE Trans. Geosci. Remote Sens.* **2001**, *39*, 8–20. [CrossRef]
57. Stoica, P.; Selen, Y. Model-order selection. *IEEE Signal Process. Mag.* **2004**, *21*, 36–47. [CrossRef]
58. Zumberge, J.F.; Heflin, M.B.; Jefferson, D.C.; Watkins, M.M.; Webb, F.H. Precise Point Positioning for the Efficient and Robust Analysis of GPS Data from Large N etworks. *J. Geophys. Res. Solid Earth* **1997**, *102*, 5005–5017. [CrossRef]
59. Gandolfi, S.; Tavasci, L.; Poluzzi, L. Improved PPP Performance in Regional Networks. *GPS Solut.* **2016**, *20*, 485–497. [CrossRef]
60. Blewitt, G.; Lavallée, D. Effect of Annual Signals on Geodetic Velocity. *J. Geophys. Res. Solid Earth* **2002**, *107*, ETG 9-1–ETG 9-11. [CrossRef]
61. Barbarella, M.; Gandolfi, S.; Poluzzi, L.; Tavasci, L. Precision of PPP as a Function of the Observing-Session Duration. *IEEE Trans. Aerosp. Electron. Syst.* **2018**, *54*, 2827–2836. [CrossRef]
62. Boehm, J.; Werl, B.; Schuh, H. Troposphere Mapping Functions for GPS and Very Long Baseline Interferometry from European Centre for Medium-Range Weather Forecasts Operational Analysis Data. *J. Geophys. Res. Solid Earth* **2006**, *111*, 2005JB003629. [CrossRef]
63. Altamimi, Z. *EUREF Technical Note 1: Relationship and Transformation Between the International and the European Terrestrial Reference Systems*; Technical Report; Institut National de l'Information Géographique et Forestière (IGN): Forestière, France, 2024.
64. Bischoff, C.A.; Ferretti, A.; Novali, F.; Uttini, A.; Giannico, C.; Meloni, F. Nationwide Deformation Monitoring with SqueeSAR® using Sentinel-1 Data. *Proc. Int. Assoc. Hydrol. Sci.* **2020**, *382*, 31–37. [CrossRef]
65. Herring, T. MATLAB Tools for viewing GPS velocities and time series. *GPS Solut.* **2003**, *7*, 194–199. [CrossRef]
66. Ferretti, A.; Savio, G.; Barzaghi, R.; Borghi, A.; Musazzi, S.; Novali, F.; Prati, C.; Rocca, F. Submillimeter Accuracy of InSAR Time Series: Experimental Validation. *IEEE Trans. Geosci. Remote Sens.* **2007**, *45*, 1142–1153. [CrossRef]
67. Stramondo, S.; Saroli, M.; Tolomei, C.; Moro, M.; Doumaz, F.; Pesci, A.; Loddo, F.; Baldi, P.; Boschi, E. Surface movements in Bologna (Po Plain—Italy) detected by multitemporal DInSAR. *Remote Sens. Environ.* **2007**, *110*, 304–316. [CrossRef]
68. Marcaccio, M.M.M. *Monitoraggio dei Movimenti Verticali del Suolo e Aggiornamento Della Cartografia di Subsidenza Nella Pianura dell'Emilia-Romagna. Periodo 2016–2021*; Technical Report; Regione Emilia–Romagna, Arpae Emilia-Romagna: Bologna, Italy, 2023.
69. Bissoli, R.P.I. *Rilievo Della Subsidenza Nella Pianura Emiliano–Romagnola. Relazione Finale, Seconda Fase*; Technical Report; Regione Emilia–Romagna, Arpa Emilia-Romagna: Bologna, Italy, 2018.

Disclaimer/Publisher's Note: The statements, opinions and data contained in all publications are solely those of the individual author(s) and contributor(s) and not of MDPI and/or the editor(s). MDPI and/or the editor(s) disclaim responsibility for any injury to people or property resulting from any ideas, methods, instructions or products referred to in the content.